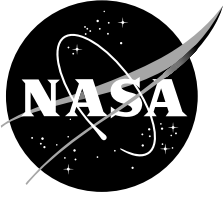**NASA/TM–2005-213454**

Computational Fluid Dynamics Analysis for the Orbiter LH$_2$ Feedline Flowliner

Cetin C. Kiris
Ames Research Center, Moffett Field, California

May 2005

The NASA STI Program Office . . . in Profile

Since its founding, NASA has been dedicated to the advancement of aeronautics and space science. The NASA Scientific and Technical Information (STI) Program Office plays a key part in helping NASA maintain this important role.

The NASA STI Program Office is operated by Langley Research Center, the Lead Center for NASA's scientific and technical information. The NASA STI Program Office provides access to the NASA STI Database, the largest collection of aeronautical and space science STI in the world. The Program Office is also NASA's institutional mechanism for disseminating the results of its research and development activities. These results are published by NASA in the NASA STI Report Series, which includes the following report types:

- TECHNICAL PUBLICATION. Reports of completed research or a major significant phase of research that present the results of NASA programs and include extensive data or theoretical analysis. Includes compilations of significant scientific and technical data and information deemed to be of continuing reference value. NASA's counterpart of peer-reviewed formal professional papers but has less stringent limitations on manuscript length and extent of graphic presentations.

- TECHNICAL MEMORANDUM. Scientific and technical findings that are preliminary or of specialized interest, e.g., quick release reports, working papers, and bibliographies that contain minimal annotation. Does not contain extensive analysis.

- CONTRACTOR REPORT. Scientific and technical findings by NASA-sponsored contractors and grantees.

- CONFERENCE PUBLICATION. Collected papers from scientific and technical conferences, symposia, seminars, or other meetings sponsored or cosponsored by NASA.

- SPECIAL PUBLICATION. Scientific, technical, or historical information from NASA programs, projects, and missions, often concerned with subjects having substantial public interest.

- TECHNICAL TRANSLATION. English-language translations of foreign scientific and technical material pertinent to NASA's mission.

Specialized services that complement the STI Program Office's diverse offerings include creating custom thesauri, building customized databases, organizing and publishing research results . . . even providing videos.

For more information about the NASA STI Program Office, see the following:

- Access the NASA STI Program Home Page at *http://www.sti.nasa.gov*

- E-mail your question via the Internet to help@sti.nasa.gov

- Fax your question to the NASA Access Help Desk at (301) 621-0134

- Telephone the NASA Access Help Desk at (301) 621-0390

- Write to:
  NASA Access Help Desk
  NASA Center for AeroSpace Information
  7121 Standard Drive
  Hanover, MD 21076-1320

NASA/TM–2005-213454
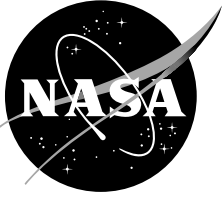
Computational Fluid Dynamics Analysis for the Orbiter LH$_2$ Feedline Flowliner

Cetin C. Kiris
Ames Research Center, Moffett Field, California

National Aeronautics and
Space Administration

Ames Research Center
Moffett Field, California 94035-1000

May 2005

Acknowledgments

The author is grateful to Dr. William Chan for his help in developing the computational grid, to Alex Tee for his help in CAD work, to Jeff Housman for his help in parametric studies for boundary conditions, and to Tim Sandstrom and David Ellsworth for their help in the visualization work. I would also like to thank Dr. Dochan Kwak for helpful discussions.

TABLE OF CONTENTS

COMPUTATIONAL FLUID DYNAMICS ANALYSIS FOR THE ORBITER LH$_2$ FEEDLINE FLOWLINER

Cetin C. Kiris

Ames Research Center

INTRODUCTION

Flow unsteadiness originating from the orbiter Low-Pressure-Fuel-Turbopump (LPFTP) inducer is one of the major contributors to the high frequency cyclic loading that results in high cycle fatigue damage to the gimbal flowliners just upstream of the LPFTP. The reverse flow generated at the tip of the inducer blades travels upstream and interacts with the bellows cavity. During phase I, the NESC Flowliner Independent Technical Assessment (ITA) team developed various computational models and carried out high-fidelity computations in order to characterize various aspects of the flow field near the flowliner. Results including 14 inducer rotations of a straight pipe model with the LPFTP inducer and 5.5 inducer rotations of the LPFTP inducer with the addition of upstream and downstream flowliners including 38 slots, an overhang area between the liners, and the bellows cavity, have been reported. The incompressible Navier-Stokes flow solver based on the artificial compressibility method was used to compute the flow of liquid hydrogen in each test article. All computations included tip leakage effects with a radial tip clearance of 0.006 in., a pump operating condition of 104.5% RPL power-level, a mass flow rate of 154.7 lbm/sec, and a rotational speed of 15,761 RPM. The findings include a significant time-periodic back-flow generated by the inducer reaching 15-20% of the tip velocity and a jet flow of 10-15% of the inducer tip speed, which penetrates into the bellows cavity creating an unsteady recirculation region in the cavity. The reverse flow and unsteady recirculation regions create an unsteady interaction between the duct and the bellows cavity resulting in high frequency cycle loading. The back flow also creates swirl in the bellows cavity on the order of 10% of the inducer tip velocity.

In phase II, the LPFTP inducer with flowliner geometry is further analyzed and 12 inducer rotations have been completed to better represent the time-periodic nature of the flow field. A parametric study is performed to compare the flow field of the original and proposed modifications to the upstream and downstream slots. The proposed modifications would entail enlargement by polishing 0.05 in. to eliminate cracks. The purpose of this study is to determine if significant changes to the flow field would occur due to the enlarged slots. Additionally, the flow through the orbiter fuel feedline manifold and the flow through the A1 test article are computed. The objective of simulating the flow field through the manifold and A1 test stand is to characterize the similarities and differences between the two configurations.

COMPUTATIONAL MODELS

The computational grid system representing the GTA test article consists of a straight inflow pipe of 48 in., the flowliner component, followed by the inducer component. The grid system includes 38 upstream slots, 38 downstream slots, and the overhang area between liners and the bellows cavity. It consists of 264 overlapping grids with 65.9 Million grid points. Details of the grid system are shown in figure 1. The flowliner component consists of an axisymmetric chamber around the external wall of the pipe, and two rows of slots in the
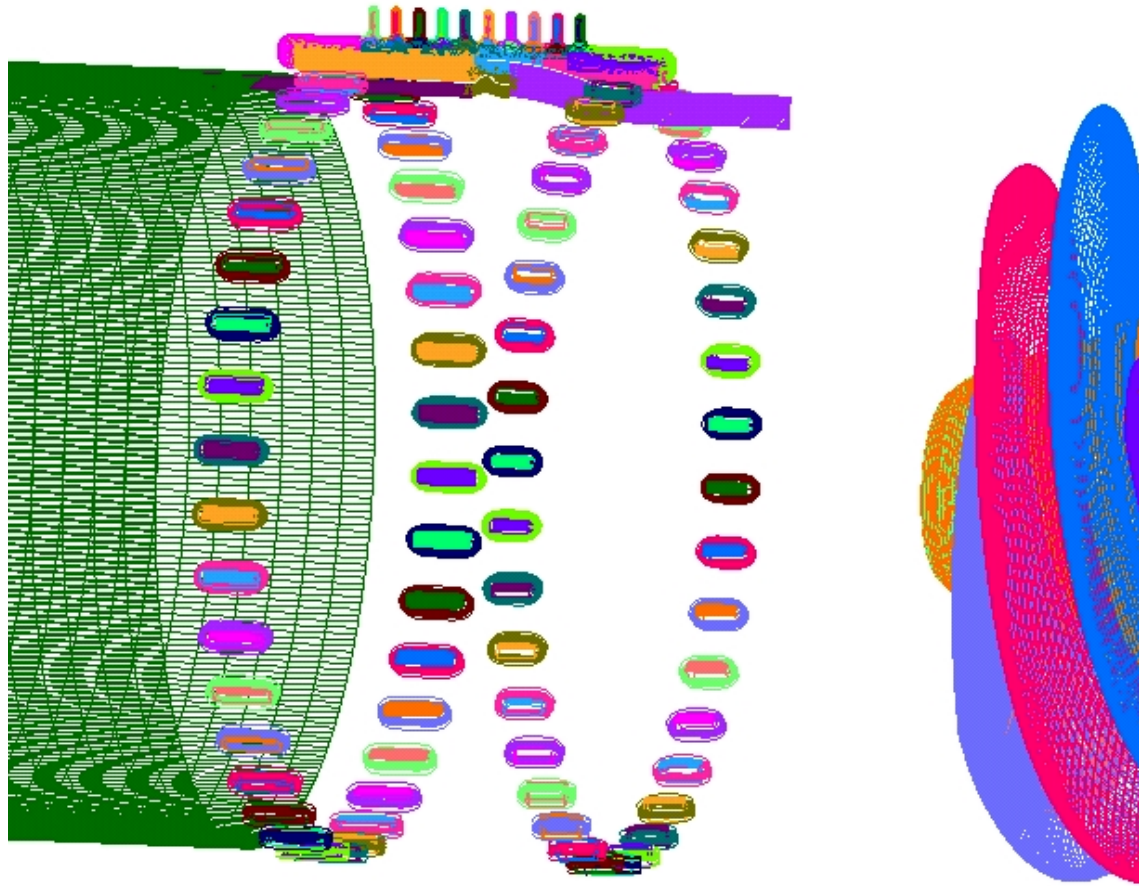
(a)
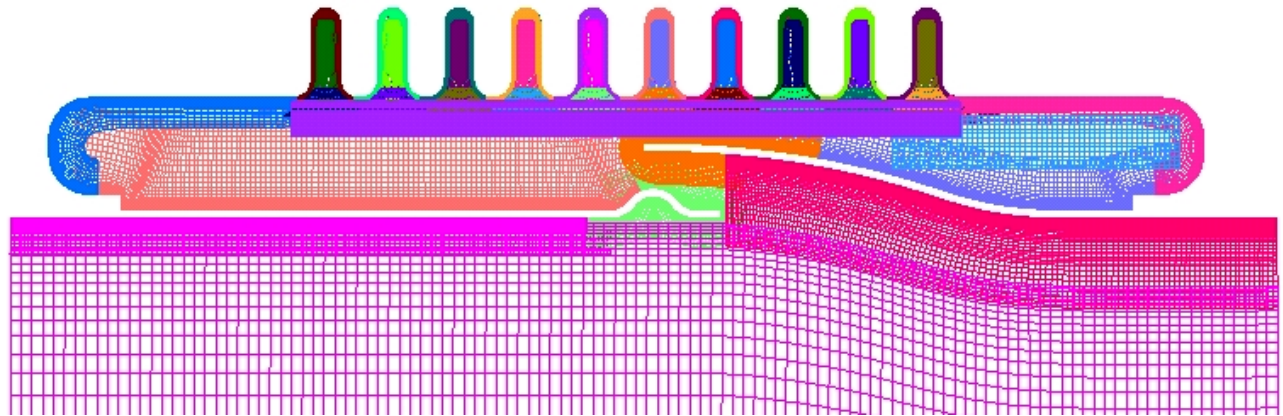
(b)

Figure 1. (a) Surface grids for LPFTP inducer and the Liquid LH$_2$ flowliner. **(b)** Details of the flowliner overset grid system.

streamwise direction. Each slot is a rectangular shaped hole with rounded corners. On the outside wall of the chamber are the bellows which are shaped like 10 periods of a sine wave. The bellows cavity is connected to the duct via the overhang area and the slots. Two-dimensional overset grids are first created for the bellows,

side walls, and the overhang area of the bellows cavity. These are then revolved 360 deg to form the volume grids. Each slot consists of a body-conforming grid and a warped Cartesian core grid in the middle of the hole. The flowliner component alone contains 212 grids and 41 Million points.

In order to speed up and automate the grid generation procedure, a script system has been developed to automatically and rapidly perform the various steps of the grid generation process prior to the use of the flow solver. Special procedures were developed to automatically create grids for each component type. The types included in the script are Blade, Pipe, Ring, Nose, Flowliner, and Strut. The Blade component is one of the most common parts of a liquid rocket subsystem and may contain multiple sections of one or more sets of different blades (e.g., inducer, impeller, diffuser). The Pipe and Ring components are used to connect different blade components. Pipes can be straight or curved and are bounded by the shroud. Rings can only be straight and are bounded by both the hub and the shroud. The Nose component is a cap that fits at the start or end of the hub. The Flowliner is a highly complex part with bellows, and slots. The Strut component consists of multiple blades connected to brackets at the shroud end and a central hub at the other end. The strut component was not used in the GTA article; it was used in the flight configuration which was not included in this report.

A separate computational model was generated for the A1 test stand. The A1 test stand (see fig. 2(a)), at Stennis Space Center, was modified in the 1970s to test a single Space Shuttle Main Engine at a time. Hydrogen and oxygen tanks are mounted at the top of the facility. The fuel flows through 12-in. "S" shaped vacuum jacketed pipes to the engine. Starting at the inlet, there is a vertical section which descends approximately 5 ft that is joined to an 80-deg elbow. Following the elbow there are two flow straighteners made of 2-in. pipe which prepares the flow for the facility turbine flowmeter located in the nearly horizontal straight section. After the flowmeter, there is another 80-deg elbow which is joined to a butterfly valve. Another straight section descends to an expansion joint and Frantz screen, followed by facility instrumentation ports. Finally the exit of the pipe is designed to bolt directly to the inlet of the Low Pressure Fuel Turbo Pump (LPFTP), without the gimbal joint. Before the BTA test was run, pressure instrumentation was added about 5.5 in. upstream of the turbo pump flange. The runs with this data are referred to as the "straight duct" runs. In order to accommodate the BTA and GTA test articles, the last section of pipe was shortened to make room for the test articles. The computational grid representing the A1 test stand is created using O-H grids consisting of six overlapping zones and a total of 7.1 Million grid points.

The orbiter fuel feedline manifold grid system consists of an inflow pipe, the manifold, three exit pipes with elbows to the main engines, and two short exit pipes; one for the re-circulating pump and the other for the fill and drain line. The re-circulating pump and fill and drain line are not included in the computational model so we have closed these two exit pipes. All pipes are connected to the manifold via internal collar grids. The upstream side of the inflow pipe and the downstream side of the exit pipes are modeled by body-conforming O-grids with a singular polar axis running down the core of the pipe. In the regions of the inflow and exit pipes that are near the manifold, the singular axis is avoided by adding a warped Cartesian core grid. Body-conforming grids are used for the walls of the manifold. A series of uniform Cartesian grids are used to occupy the core of the manifold. The entire grid system consists of 38 grids and 12 Million points (see figs. 2(b) and 2(c)). The computational model for the A1 test stand does not include the flow straighteners, flowmeter, butterfly valve, or the frantz screen because the geometry definition was not available for these parts. The computational model for the orbiter manifold feed system does not include the pre-valves that are downstream of the manifold in each engine feed. The manifold model also does not include the struts, the flowliners, or the LPFTP.
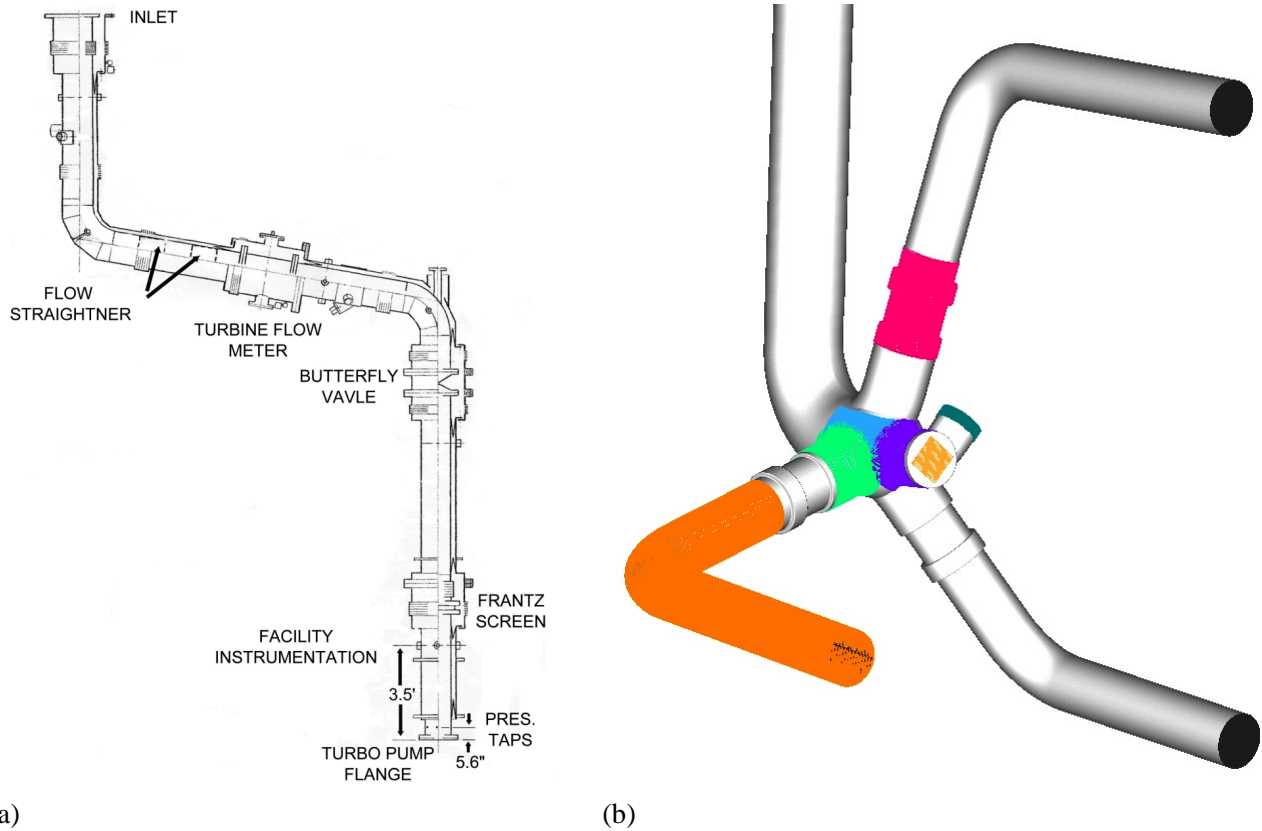
Figure 2. (a) Schematic of A1 test stand. **(b)** Details of orbiter fuel feedline manifold.

NUMERICAL METHOD

The present computations are performed utilizing the INS3D computer code, which solves the incompressible Navier-Stokes equations for both steady-state and unsteady flows. The numerical solution of the incompressible Navier-Stokes equations requires special attention in order to satisfy the divergence-free constraint on the velocity field. The incompressible formulation does not explicitly yield the pressure field from an equation of state or the continuity equation. One way to avoid the difficulty of the elliptic nature of the equations is to use an artificial compressibility method, developed by Chorin (ref. 1). The artificial compressibility method introduces an artificial time-derivative of the pressure into the continuity equation. This transforms the elliptic-parabolic type partial differential equations into the hyperbolic-parabolic type. An incompressible flow solver, INS3D, has been developed (refs. 2–4) based on this algorithm. Since the convective terms of the resulting equations are hyperbolic, upwind differencing can be applied to these terms. The current version uses Roe's flux-difference splitting (ref. 5). The third and fifth-order upwind differencing used here are implementations of a class of high-accuracy flux-differencing schemes for the compressible flow equations. To obtain time-accurate solutions, the equations are iterated to convergence in pseudo-time for each physical time step until the divergence of the velocity field has been reduced below a specified tolerance value. The total number of sub-iterations required varies depending on the problem, time step size and the artificial compressibility parameter used. Typically the number ranges from 10 to 30 sub-iterations. The matrix equation is solved iteratively by using a non-factored Gauss-Seidel type line-relaxation scheme (ref. 6), which maintains stability and allows a large pseudo-time step to be taken. Current computations have been carried out using Multi-Level Parallelism (MLP) on SGI-Origin and SGI-Altix platforms.

4
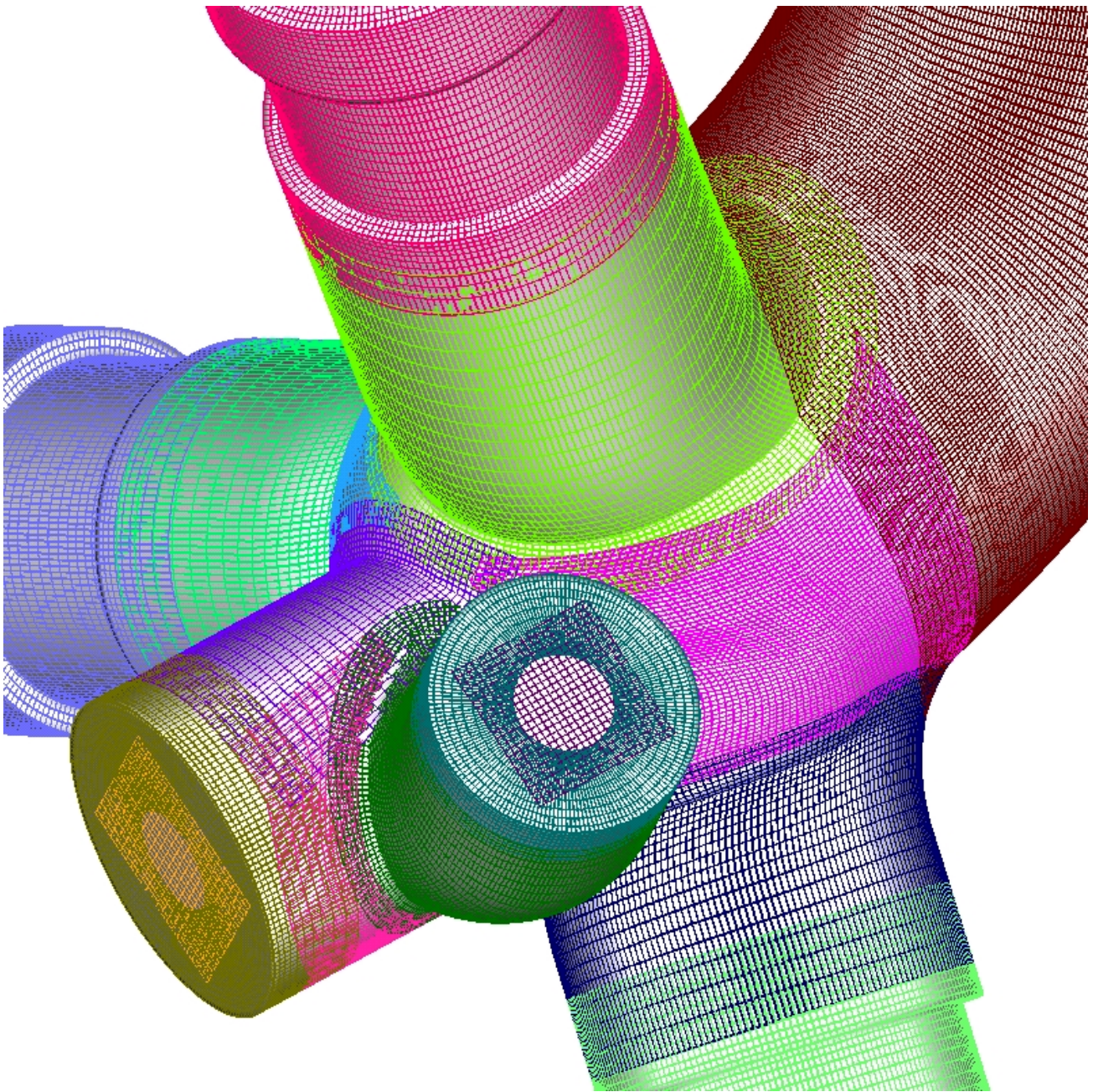
(c)

Figure 2. (c) Details of orbiter fuel feedline manifold.

COMPUTED RESULTS

Flowliner Analysis

In all computations, the inducer tip leakage effect is included with a radial tip clearance of 0.006 in. Pump operating condition is 104.5% RPL power-level with a mass flow of 154.7 lbm/sec and a rotational speed of 15,761 RPM. The problem was non-dimensionalized with a reference length of one inch and inducer tip velocity of 825.25 ft/sec. The Reynolds number for these calculations is 36 Million. Liquid Hydrogen is treated as an incompressible single phase fluid. An initial condition of flow at rest and no inducer rotation is used to start the computations. The inducer is then rotated at full speed as a start-up procedure. Mass flow is specified at the inflow and pressure is extrapolated at the outflow along with a mass-flow correction. Simulations for 12 inducer rotations were completed. In the phase I report, the detailed flow field is presented in figures 4–12 after the fifth rotation (see NESC-ITA Phase 1 Report). The qualitative behavior of the flow field is very similar after twelve inducer rotations. Rather than repeating the content of these figures for the twelfth rotation, we present instantaneous snapshots of particle traces and surface contours of axial and cross-flow velocities in a three-dimensional (3D) perspective.

In figure 3(a) particles are released from one upstream slot, one downstream slot, and from the overhang area. In figures 3(b)–3(d) the particles are released from each of the 38 downstream slots. The mean flow direction is from left to right in figures 3(a) and 3(c), towards the inducer. In figures 3(b) and 3(d) we are viewing the flowliner from the inducer. The figures are snapshots from particle trace animations that have evolved for one and a half rotations. The particles are colored by the axial velocity values ranging from –165 to +165 ft/sec (see fig. 3(a)). The particles released from both upstream and downstream slots in figure 3(a) are interacting with neighboring slots traveling from the duct to the bellows cavity and from the bellows cavity to the duct. This indicates a highly unsteady interaction between the flow field in the bellows cavity and the flow field in the duct. The swirl present in the particle trace appears to be higher in the downstream slots where particles have traced four and half slots while the upstream particles have traveled only two and half slots. The particles released from the overhang area tend to travel into the bellows cavity with the exception of a few particles traveling into the duct. In figure 3(b) we are observing the particles from the inducer's perspective where we can see the particles moving into and out of the bellows cavity through the slots. There are four regions of positive velocity particles traveling from the walls toward the center. These are particles released from the slots which do not interact with the four reverse flow regions created by the inducer. Analyzing the interior of the duct we can see the existence of the swirl near the downstream flowliner.

Examining figure 3(c) we can see that some of the particles released from the slots travel to the overhang region where they interact with the reverse flow and some of the particles become trapped in the bellows cavity. This suggests that some particles are recirculating through the overhang area into the bellows cavity and through the slots into the duct. This unsteady interaction between four backflow regions generated by the inducer and the secondary flow features in the bellows cavity lead to a break up of the 4theta forcing function in the flowliner area. Figure 3(d) suggests the existence of a 5theta forcing function, but more post-processing and future investigations should be conducted.
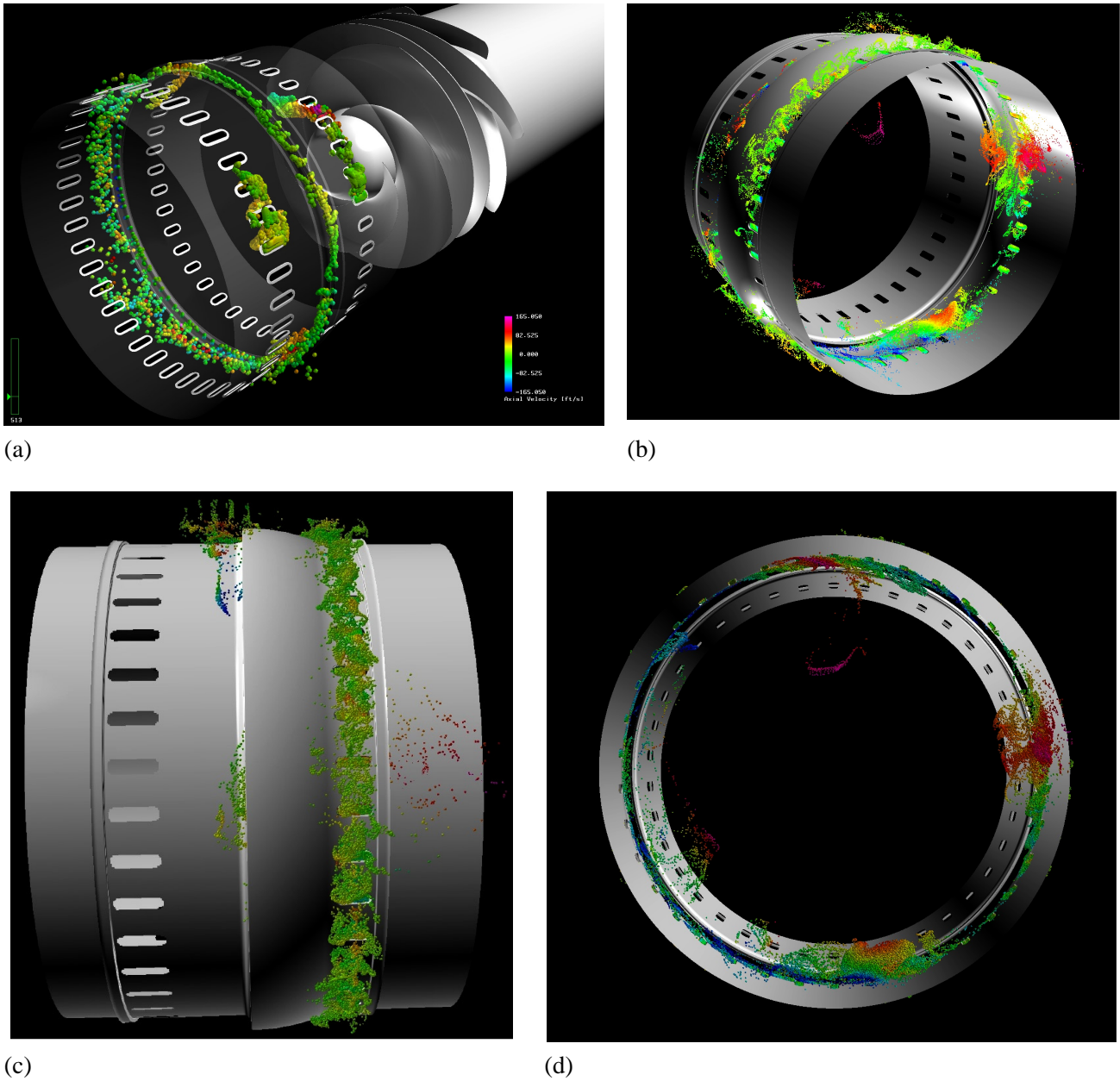
(a)

(b)

(c)

(d)

Figure 3. Instantaneous snapshots of particle traces colored by axial velocity values.

In figures 4(a) and 4(b) particles are released from the upstream slots and evolve for five inducer rotations. The color of the particles represent forward flow (blue) and backward flow (red). We see from the figures that the particles are driven towards the center of the duct and travel to the inducer where some of the particles are trapped into the backflow regions with the 4theta forcing function. In figures 4(c) and 4(d) the particles are released from the downstream slots and evolve for five rotations. In figure 4(c) the particles are colored the same as in the previous two figures. We observe a much more complicated flow structure where many of the particles travel into and out of the bellows cavity. In figure 4(d) we have multi-colored the particles with axial velocity in order to illustrate their presence in the bellows cavity. When the particles are released from the downstream slots they are under the influence of the backflow and swirl such that fewer particles travel toward the inducer.
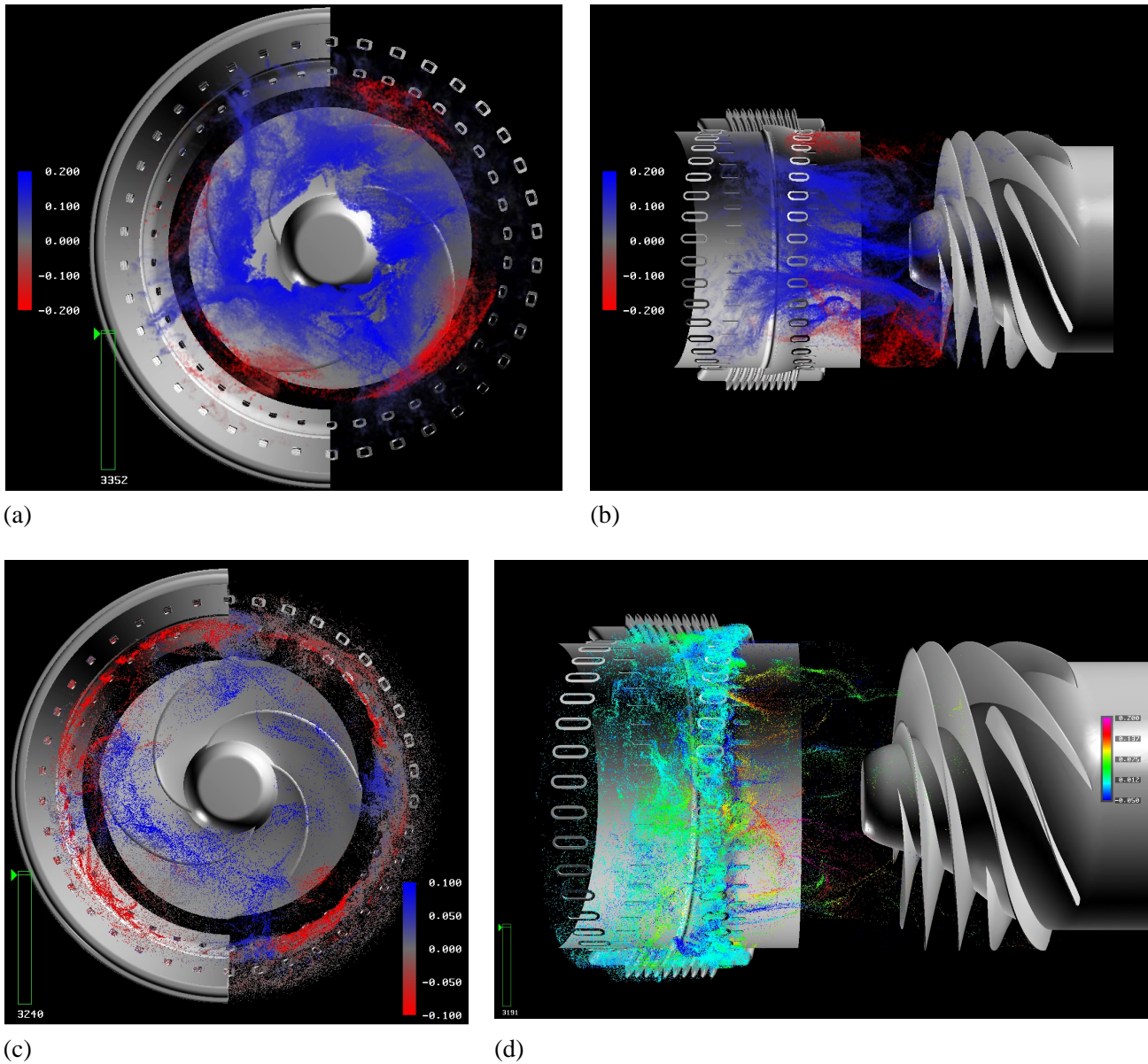
7

(a)

(b)

(c)

(d)

Figure 4. Instantaneous snapshots of particle traces colored by axial velocity values.

Figure 5 displays the axial velocity contours on a vertical plane. Due to the number of slots, which is 38 instead of 36, there is a lack of symmetry on the vertical plane. To create this figure the data on each of the structured overset grids are cut vertically and projected onto an unstructured two-dimensional surface. Inherent in this process is the creation of small discontinuities in the contours between overset grids that do not line up with one-to-one matching in the selected two-dimensional plane. The contours show strong reverse flow regions coming from the blade, traveling through the overhang region creating a jet-like flow on the order of 10% of the inducer tip speed. The backflow regions travel up from the inducer blades to the upstream flowliner.
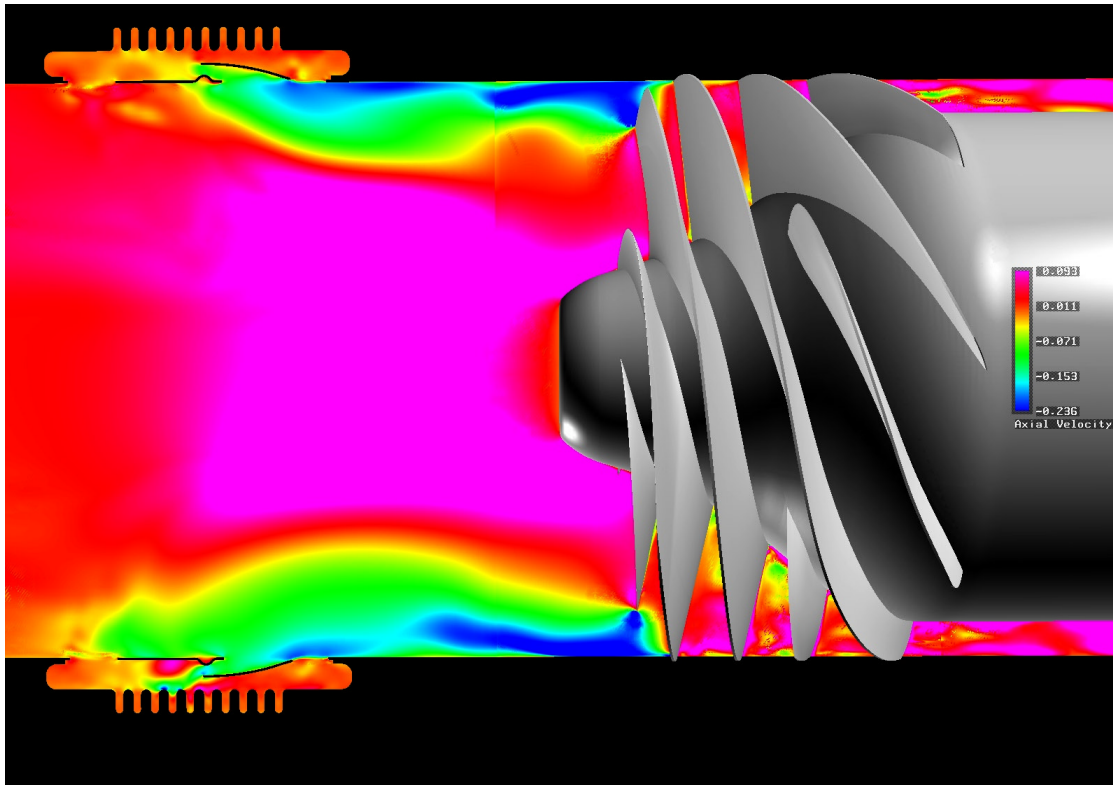
Figure 5. Instantaneous axial velocity contours on a vertical plane (12th rotation).
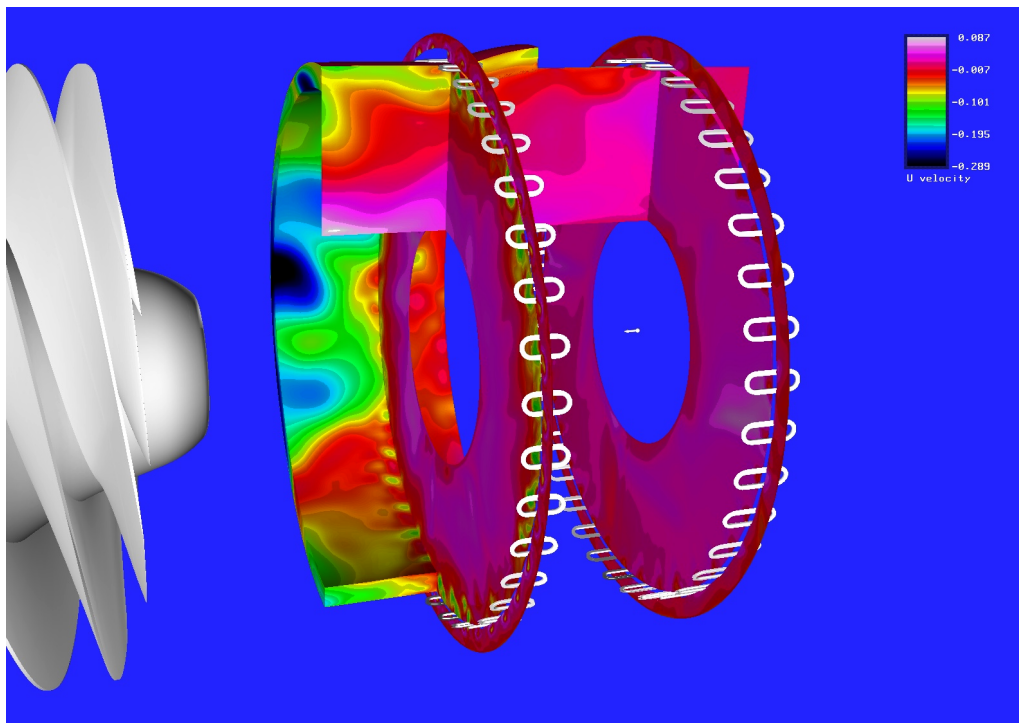

Figure 6. Instantaneous axial velocity contours on vertical, circumferential, and cross-sectional planes.

Figure 6 provides a 3D perspective of the axial flow contours displaying vertical, circumferential, and cross-sectional contour planes. Evidence of a strong reverse flow generated by the blades that travels to the upstream flowliner is seen as in the previous figure. Examining the cross-sectional contour planes surrounding the upstream and downstream flowliners, we see stronger reverse flow regions in the downstream flowliner than in the upstream flowliner. Additionally, figure 7 displays the cross-flow velocity magnitude at the same cutting planes as the previous figure. The cross-flow velocity is highest near the blades of the inducer and coincides with the largest reverse flow regions. At each of the slots of the downstream flowliner high magnitude cross-flow velocity contours are found in the bellows cavity and in the duct which provides evidence of the strong unsteady interaction of the flow through the slots between the bellows cavity and the duct. The order of magnitude of the swirl in the duct near the downstream liner is 15% of the inducer tip speed, while at the upstream liner the swirl in the duct is less than 3% of the inducer tip speed. Alternatively, the swirl maintains a higher value in the bellows cavity near the upstream flowliner. This indicates that the swirl travels through the overhang area into the bellows cavity.
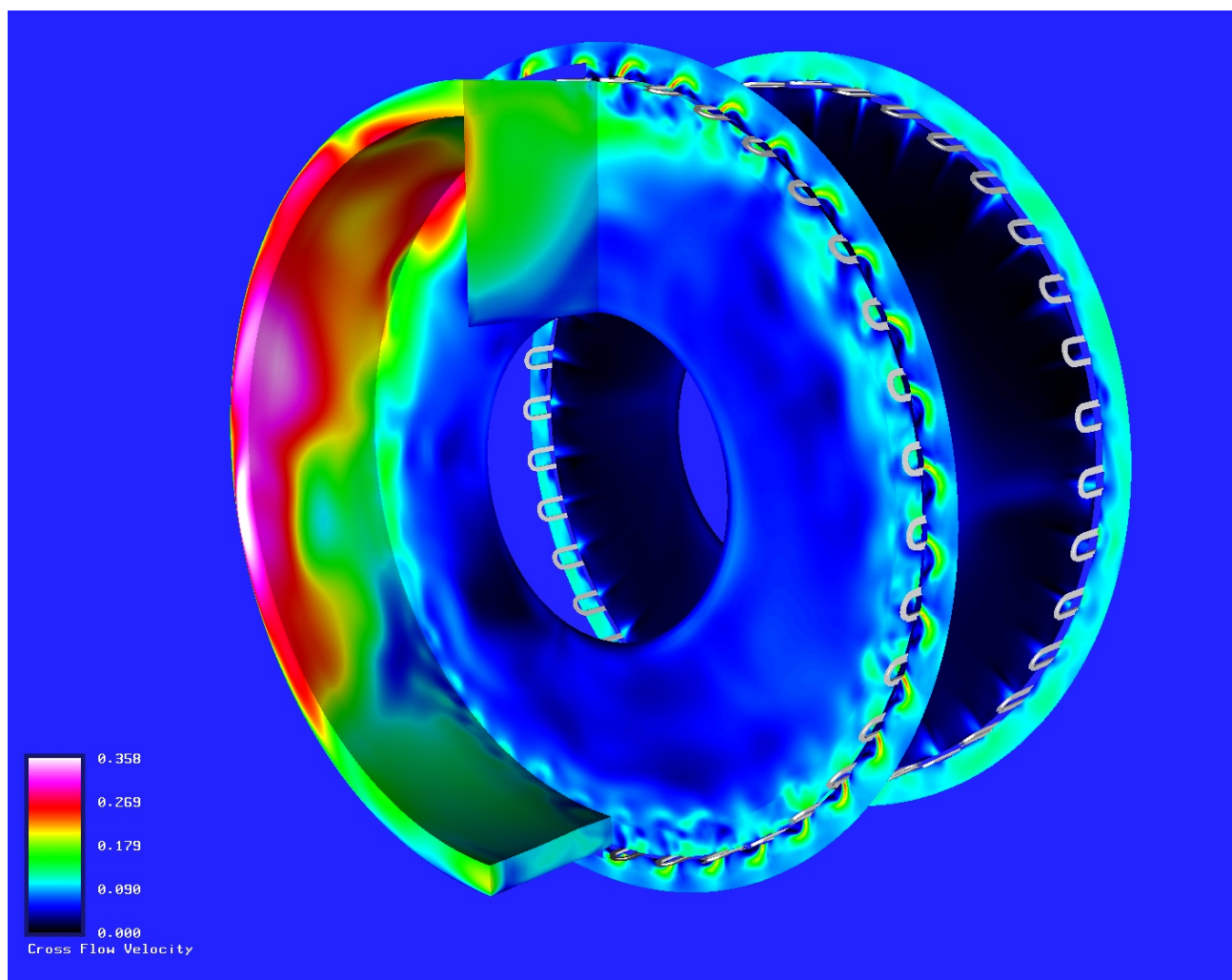

Figure 7. Cross-flow velocity magnitude at instantaneous time (12th rotation).

One of the recommendations to repair any new cracks found on the flowliners is to polish them such that the cracks are removed. This procedure makes the polished slots larger than the original size. A computational

model is created such that one upstream flowliner slot and one downstream flowliner slot is 0.05-in. larger in each direction than the neighboring slots. Initial conditions for this solution were started from the eighth inducer rotation of the original configuration. The solution is then computed for four additional inducer rotations, and the solutions for both the original and modified configurations are compared. The purpose of the two computations is to determine if the existence of slots larger than the others creates any significant differences in the flow field.

A detailed look at the velocity fields in the slots reveals some quantitative differences. In figure 8 the velocity vectors inside the original upstream liner slots are shown. Analogously, in figure 9 the velocity vectors inside the enlarged upstream slots are displayed. The larger slot is located at the center of the picture. In both designs a large velocity magnitude exists at the upstream edge of each of the slots. In the enlarged slot a slightly higher velocity magnitude region is created near the downstream edge of the slot. Qualitatively, the velocity fields are very similar and it appears that enlarging one slot does not affect the flow field in a significant way. Figures 10 and 11 show the velocity vectors at the original and enlarged downstream flowliner slots at another instantaneous time. The only noticeable difference is the appearance of a secondary flow region near the base of the enlarged slot.
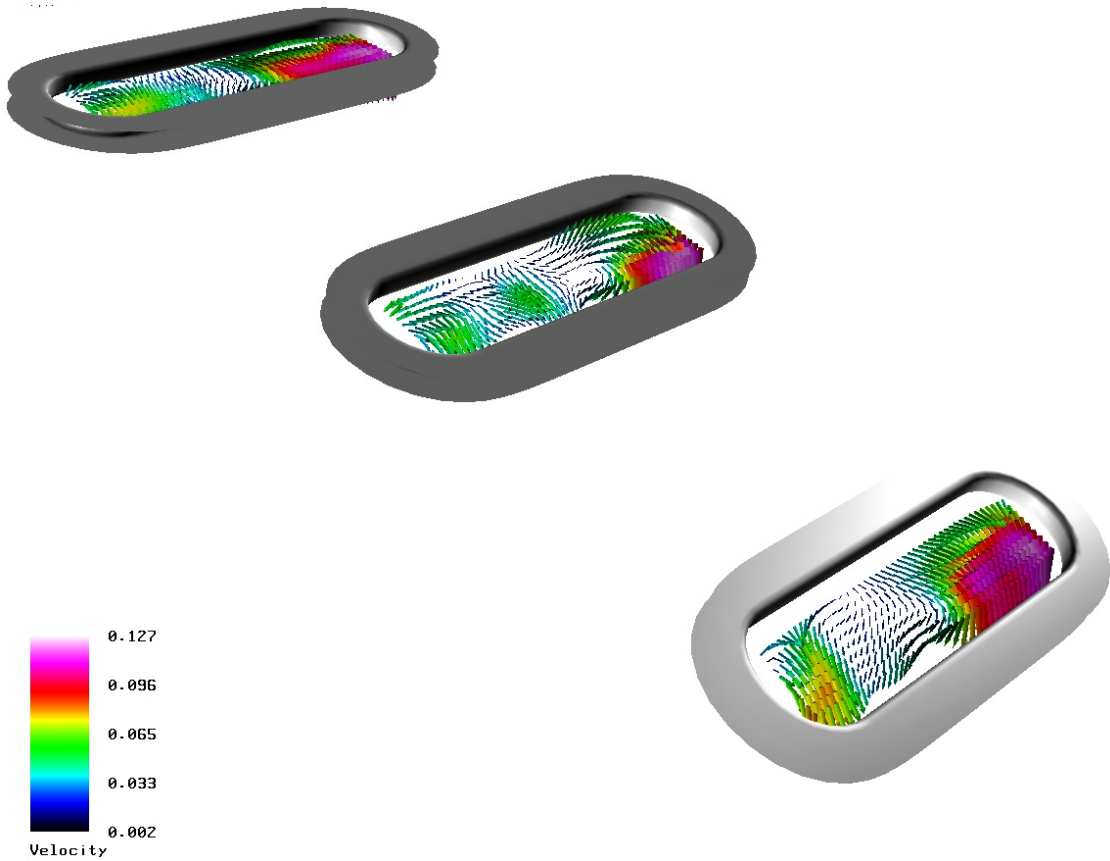

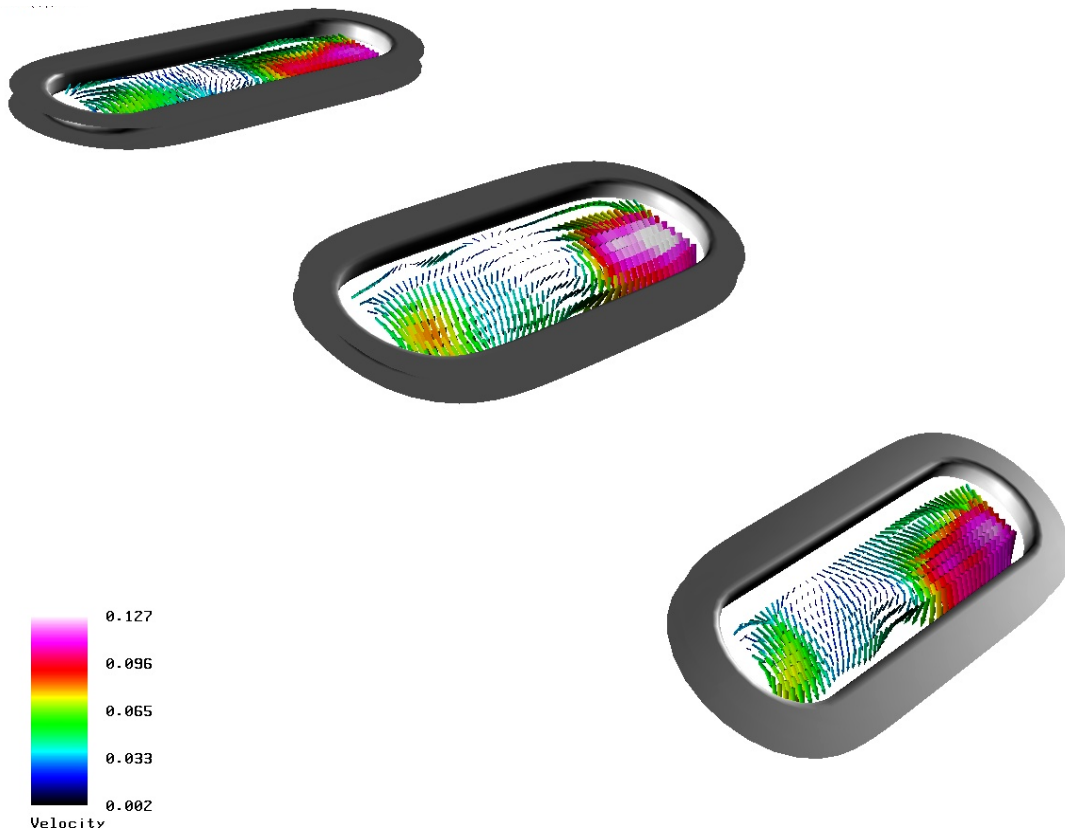**Figure 8.** Velocity vectors at instantaneous time in the upstream liner slots (original configuration).

Figure 9. Velocity vectors at instantaneous time in the upstream liner slots (one enlarged slot).
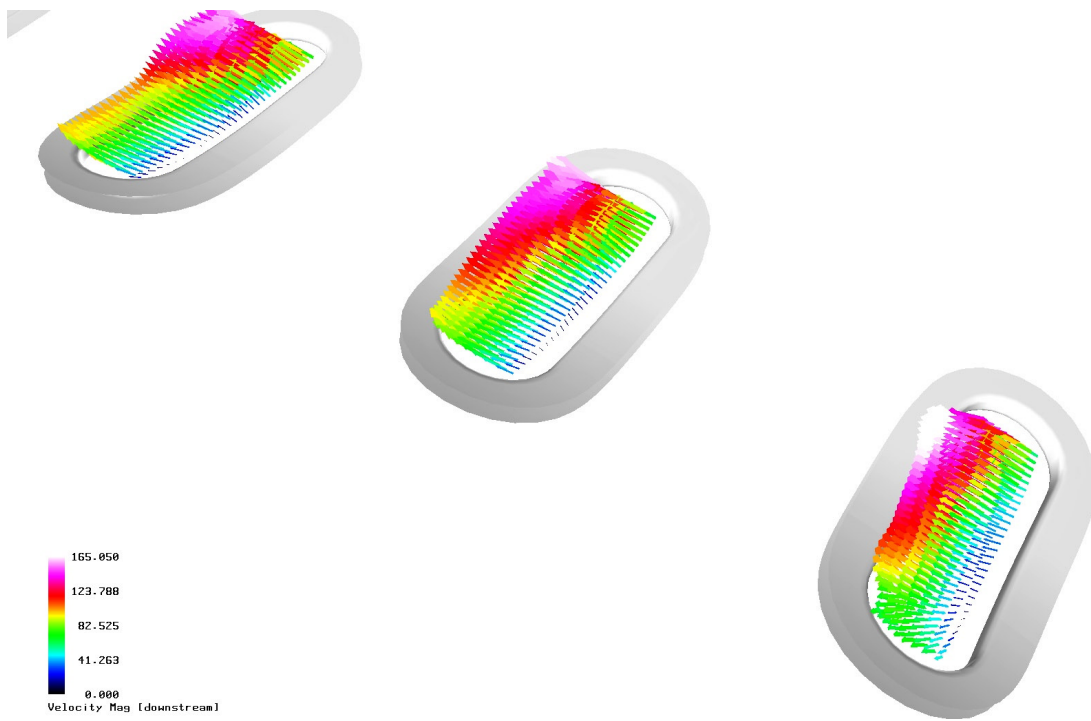

Figure 10. Velocity vectors at instantaneous time in the downstream liner slots (original configuration).
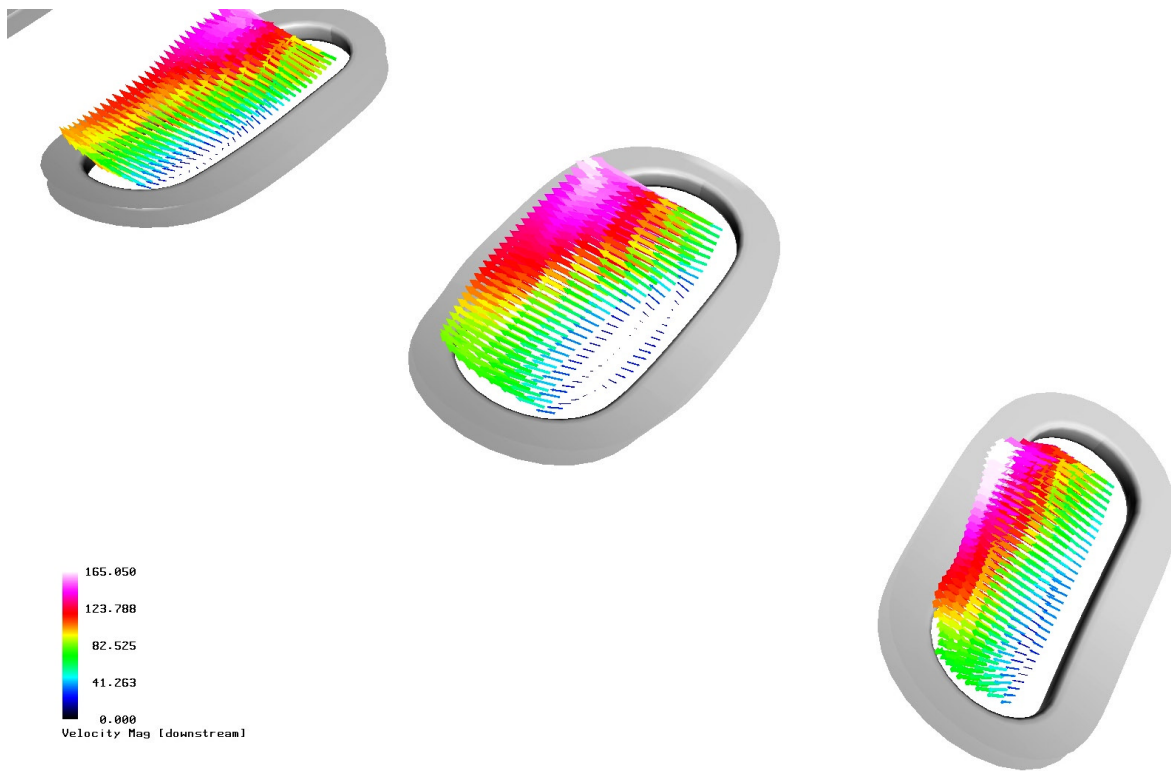
12

Figure 11. Velocity vectors at instantaneous time in the downstream liner slots (one enlarged slot).

Results obtained from the original configuration were averaged and provided to the acoustics team to help them design acoustics experiments for flowliners in order to access the effect of slot modifications on edge tones. Figure 12 shows the physical locations where the averaged quantities are obtained.

A1 Test Stand and Orbiter Manifold Analysis

Initially, steady-state calculations were conducted for both the A1 test stand and the orbiter manifold. The calculations for the orbiter manifold did not converge to a steady solution because of high grid resolution which captures the fine scale unsteady details that exist in high Reynolds number flows. Then, time-accurate calculations were performed and the mean flow results are presented here. For both of these computations the same non-dimensionalization is used as in the flowliner analysis, including a Reynolds number of 36 Million based on the inducer tip speed and the reference length of an inch. Consistent inflow and exit boundary conditions are used for the A1 test stand and the orbiter manifold, such that the A1 test stand exit and the three engines downstream of the orbiter manifold receive the same mass-flow rate. At the inflow, the mass-flow rate is specified with a corresponding turbulent velocity profile and the pressure is calculated through the characteristic relation. At the exit the pressure is extrapolated and the mass-flow rate is enforced.
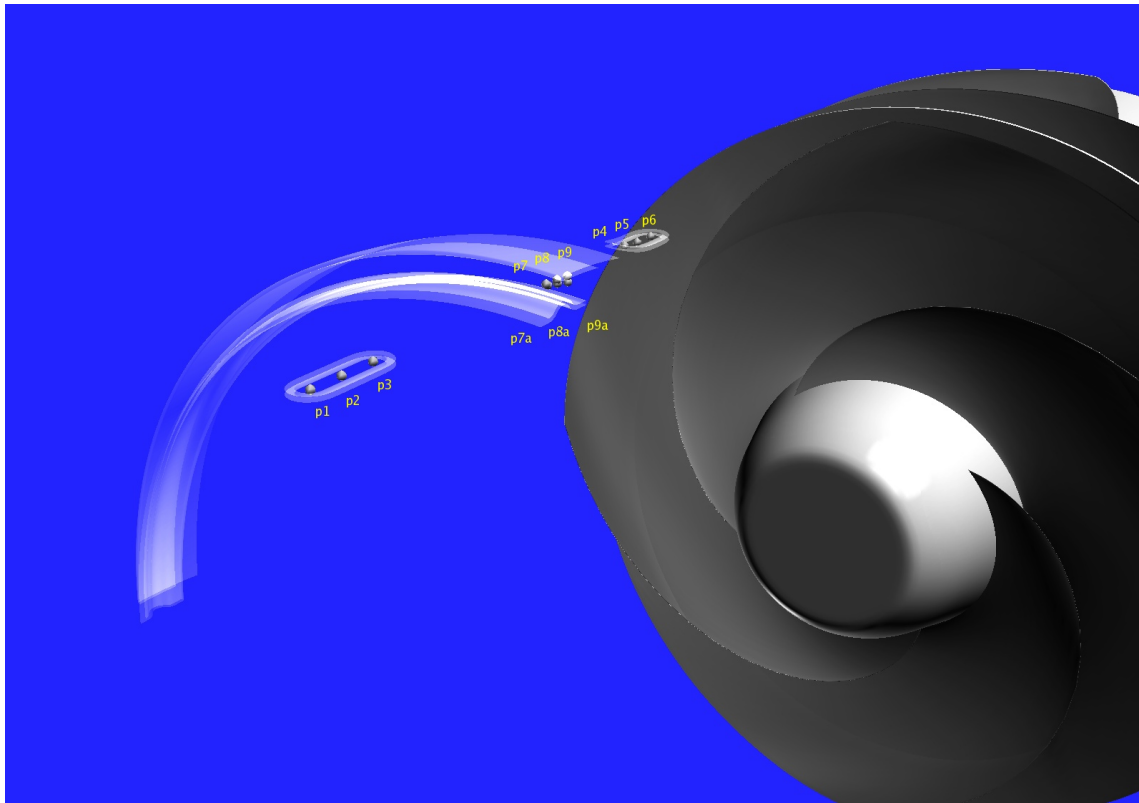
Figure 12. Location of the points where averaged velocity values are provided to acoustics team.

In figure 13 the velocity magnitude at the outlet of the A1 test stand is displayed, the contour level ranges from 0.0 to 48.0 ft/s with 12.0 ft/s intervals. The velocity profile is consistent with the turbulent velocity profile of a straight pipe; the low velocity region near the inner wall is due to the second turn. The non-dimensional delta pressure at the outlet is plotted in figure 14, where we see from the contour level range that the pressure is converged to a constant. The difference between the max and min contour levels is 5.2e-6, which corresponds to 0.0034 psi. To obtain the pressure difference in psi the non-dimensional values must be multiplied by a factor of 653. In contrast the exit velocity of the orbiter manifold displayed in figure 15 is qualitatively different for each of the three outlet sections, and none of these sections are represented well by the A1 test stand results. Figure 15 also shows that a large velocity profile has developed at the outer wall of the engine 1 feedline, while the high velocity region is better distributed around the entire wall of the engine 3 feedline, and high-low velocity regions near the walls of the engine 2 feedline are not well-developed. The exit pressure in engine 2 has converged to 1.3 psi less than the exit pressure value of engine 1 and engine 3 (see fig. 16). One of the primary reasons for the different velocity profiles and pressure contours at the three engine feedlines is the difference in lengths of the engine feedlines. Additionally the velocity profiles for each of the three engines are different as they leave the manifold.
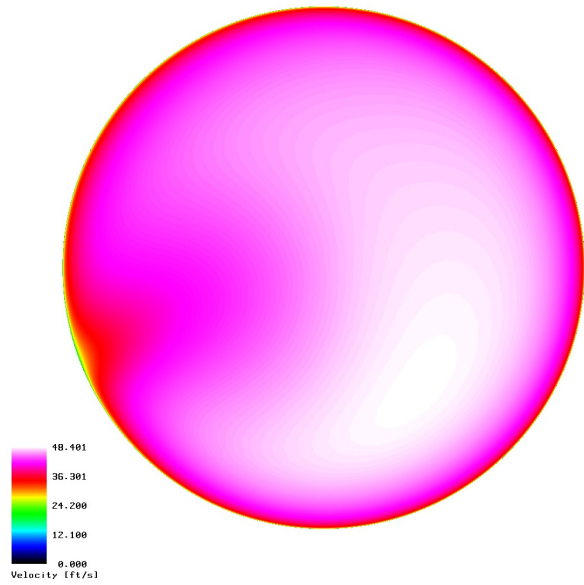
14

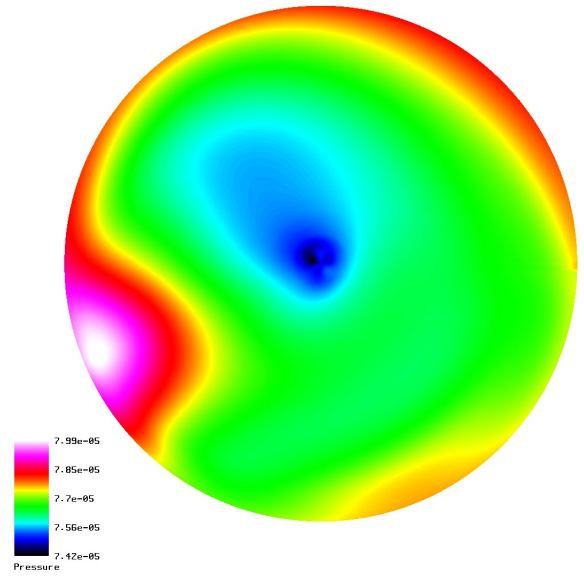**Figure 13.** Total velocity contours at the outlet of A1 test stand.

Figure 14. Pressure contours at the outlet of A1 test stand.
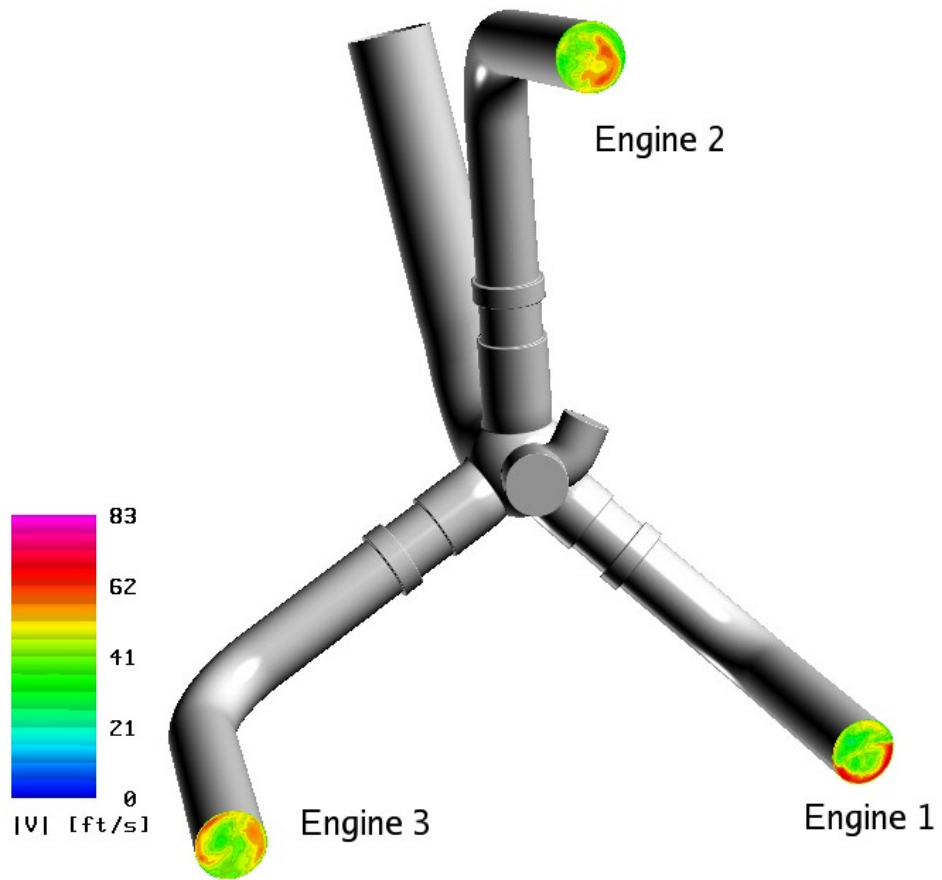

Figure 15. Total velocity magnitude contours at the outlet of the orbiter manifold and inlet to the LPFTP.
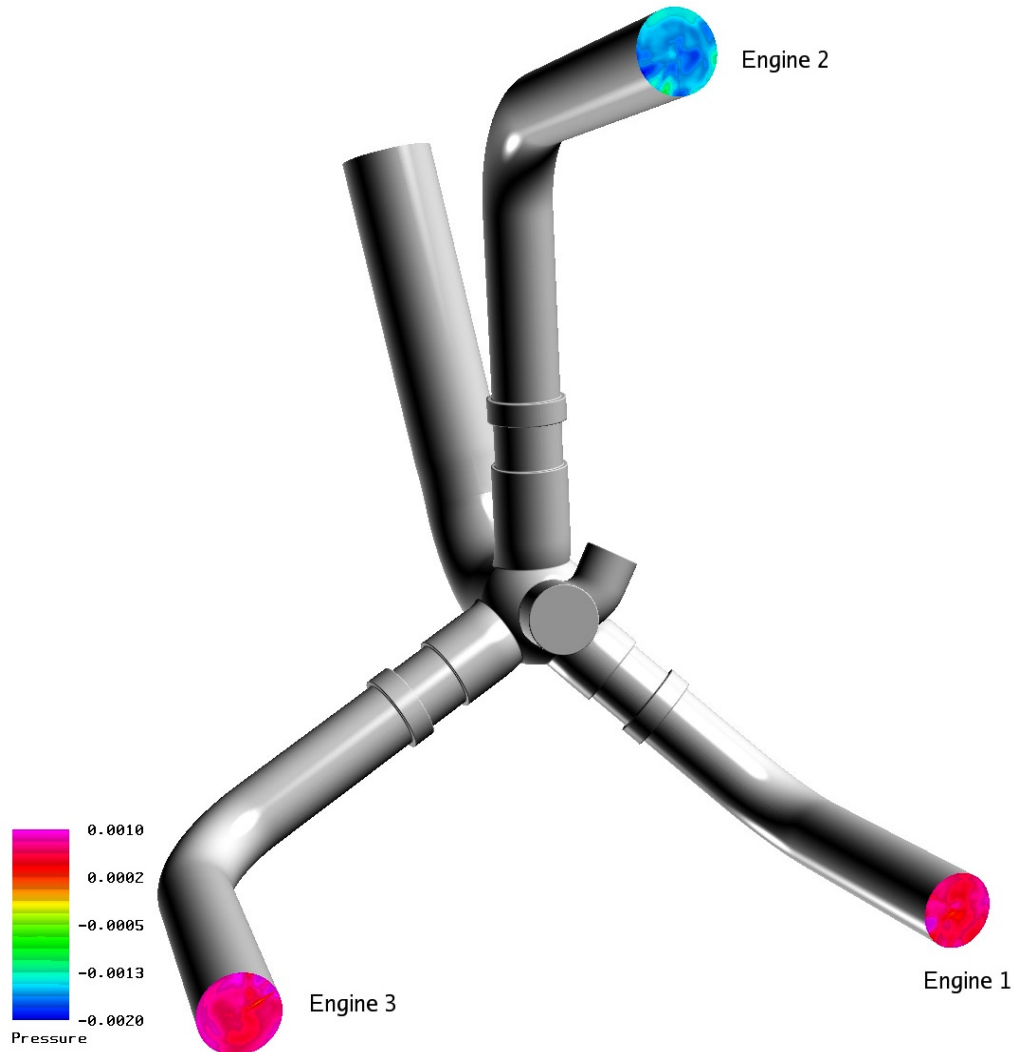
Figure 16. Delta pressure contours at the outlet of the orbiter manifold and inlet to the LPFTP.

Figure 17 displays the velocity magnitude on the vertical plane of the A1 test stand. A well-developed straight pipe turbulent profile is observed in the inlet and outlet sections. The image shows a very high to very low velocity magnitude on the inside of the first bend, while at the second bend the velocity is more uniform. Figure 18 displays the pressure profile on the vertical plane which looks similar to the pressure profile of an inviscid pipe flow; this is expected from the high Reynolds number. The vertically sliced velocity and pressure profiles obtained from the orbiter manifold solution are qualitatively different than those computed in the A1 test stand.

The velocity magnitude contours shown in figure 19 and pressure contours shown in figure 20 illustrate that each engine LPFTP receives a different inflow velocity profile and a different inlet pressure than observed for the A1 test stand.
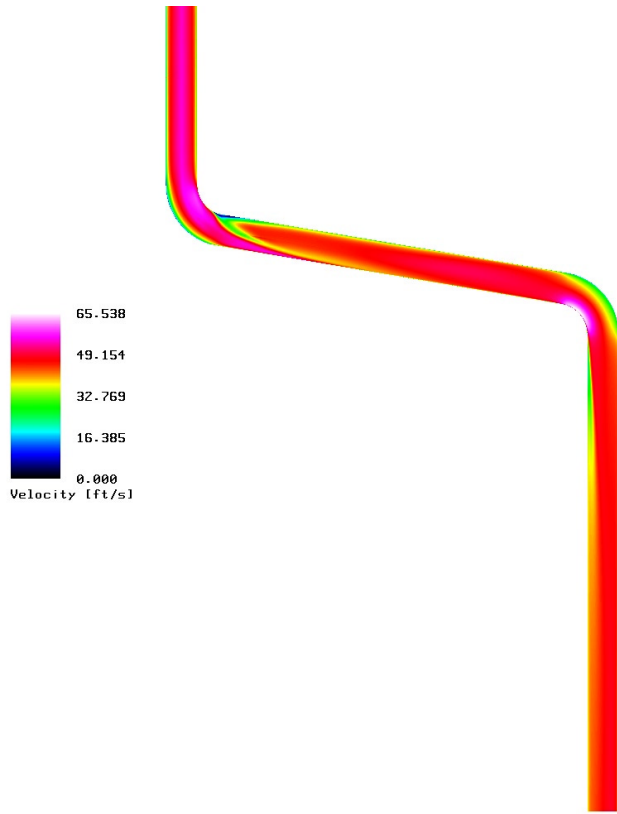
Figure 17. Total velocity magnitude contours on the vertical plane of the A1 test stand.
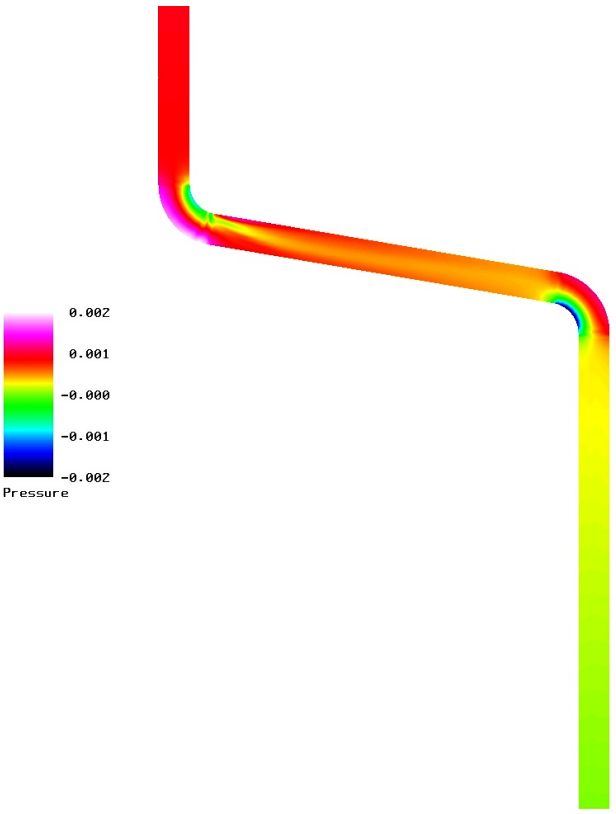

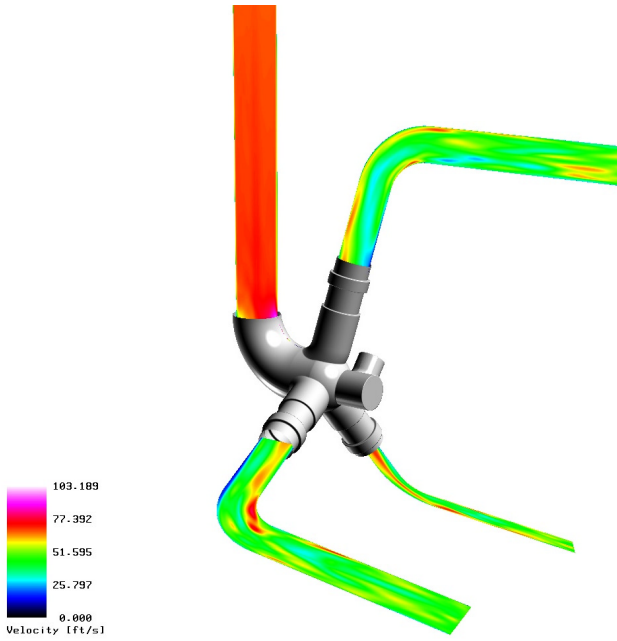**Figure 18**. Pressure contours on the vertical plane of the A1 test stand.

Figure 19. Total velocity magnitude contours on the vertical planes of the orbiter manifold.
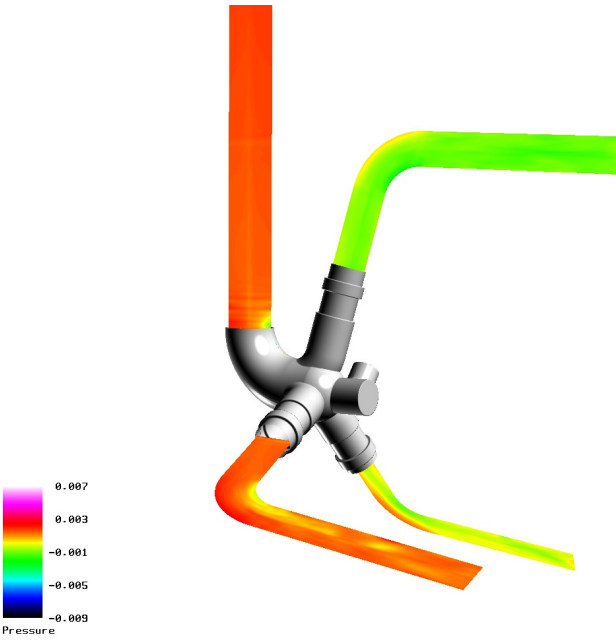
Figure 20. Pressure contours on the vertical planes of the orbiter manifold.
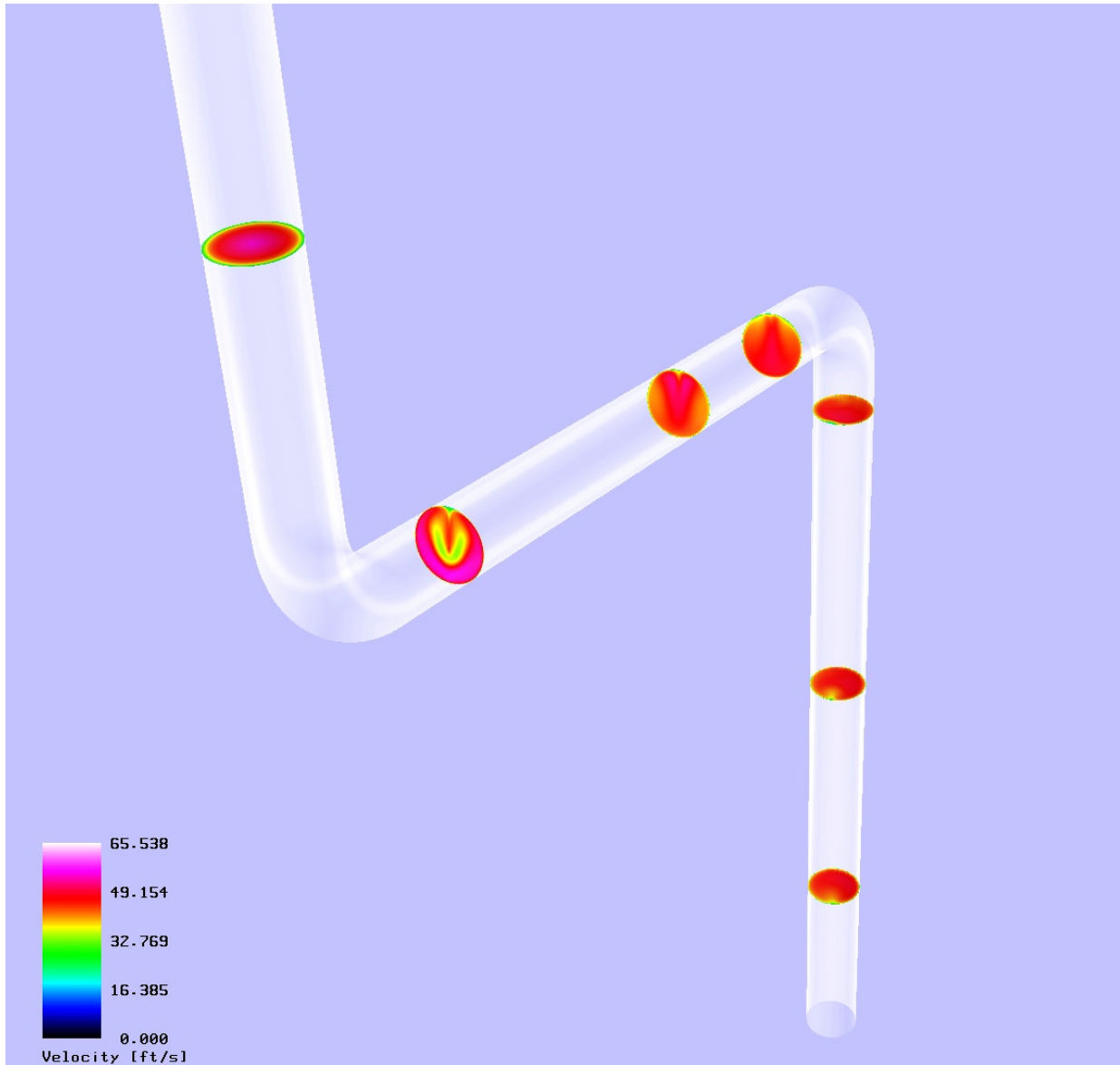
Figure 21. Total velocity magnitude contours at various cross-sections of the A1 test stand model.

In figure 21 the velocity magnitude is displayed at various cross-sections of the A1 test stand. The flow direction is from the top of the figure to the bottom. The velocity profile is uniform before the first turn. It becomes non-uniform after the first turn, but returns to a more uniform distribution toward the end of the pipe.

SUMMARY

In phase II, additional inducer rotations are simulated in order to understand the root cause of the flowliner crack problem. CFD results confirmed that there is a strong unsteady interaction between the backflow regions caused by the LPFTP inducer and secondary flow regions in the bellows cavity through the flowliner slots. It is observed that the swirl on the duct side of the downstream flowliner is stronger than on the duct side of the upstream flowliner. Due to this swirl, there are more significant unsteady flow interactions through the downstream slots than those observed in the upstream slots. Averaged values of the local velocity at the slots were provided to the NESC-ITA flow physics acoustics team to guide them in designing the acoustics experiment. A parametric study was performed to compare the flow field in the flowliner area when one upstream slot and one corresponding downstream slot were enlarged. No significant differences were observed between the flow field obtained from the enlarged slot configuration when compared with the original configuration. More cases must be analyzed with various enlarged slot configurations to generalize this observation. The flow through the A1 test stand and the flow through the orbiter fuel feedline manifold were simulated without the LPFTP. It was observed that incoming flow to the flowliner and inducer was more uniform in the A1 test stand then in the orbiter manifold. Additionally, each engine LPFTP in the orbiter receives significantly different velocity distributions. Because of these differences observed in the computed results it is not possible for the A1 test stand to represent the three different engine feedlines simultaneously.

REFERENCES

1. Chorin, A. J.: A Numerical Method for Solving Incompressible Viscous Flow Problems. J. of Comp. Phys., vol. 2, 1967, pp. 12–26.
2. Kiris, C.; and Kwak, D.: Parallel Unsteady Turbopump Simulations for Reusable Launch Vehicle. Frontiers of Computational Fluid Dynamics 2002, Caughey, D. A. and Hafez, M., eds., World Scientific, 2002.
3. Kiris, C.; Kwak, D.; and Rogers, S.: Incompressible Navier-Stokes Solvers in Primitive Variables and Their Applications to Steady and Unsteady Flow Simulations. Numerical Simulations of Incompressible Flows, Hafez, M., ed., World Scientific, 2003.
4. Rogers, S. E.; Kwak, D.; and Kiris, C.: Numerical Solution of the Incompressible Navier-Stokes Equations for Steady and Time-Dependent Problems. AIAA Journal, vol. 29, no. 4, 1991, pp. 603–610.
5. Roe, P. L.: Approximate Riemann Solvers, Parameter Vectors, and Difference Schemes. J. of Comp. Phys., vol. 43, 1981, pp. 357–372.
6. MacCormack, R. W.: Current Status of Numerical Solutions of the Navier-Stokes Equations. AIAA Paper 85-0032, AIAA Aerospace Sciences Meeting, Reno, NV, Jan. 14–17, 1985.

REPORT DOCUMENTATION PAGE

Form Approved
OMB No. 0704-0188

The public reporting burden for this collection of information is estimated to average 1 hour per response, including the time for reviewing instructions, searching existing data sources, gathering and maintaining the data needed, and completing and reviewing the collection of information. Send comments regarding this burden estimate or any other aspect of this collection of information, including suggestions for reducing this burden, to Department of Defense, Washington Headquarters Services, Directorate for information Operations and Reports (0704-0188), 1215 Jefferson Davis Highway, Suite 1204, Arlington, VA 22202-4302. Respondents should be aware that notwithstanding any other provision of law, no person shall be subject to any penalty for failing to comply with a collection of information if it does not display a currently valid OMB control number.
PLEASE DO NOT RETURN YOUR FORM TO THE ABOVE ADDRESS.

1. REPORT DATE *(DD-MM-YYYY)* 20-05-2005	2. REPORT TYPE Technical Memorandum	3. DATES COVERED *(From - To)*

4. TITLE AND SUBTITLE

Computational Fluid Dynamics Analysis for the Orbiter LH_2 Feedline Flowliner

5a. CONTRACT NUMBER

5b. GRANT NUMBER

5c. PROGRAM ELEMENT NUMBER

6. AUTHOR(S)
Cetin C. Kiris

5d. PROJECT NUMBER

5e. TASK NUMBER

5f. WORK UNIT NUMBER
21-656

7. PERFORMING ORGANIZATION NAME(S) AND ADDRESS(ES)
Ames Research Center
Moffett Field, CA 94035-1000

8. PERFORMING ORGANIZATION REPORT NUMBER
A-0513361

9. SPONSORING/MONITORING AGENCY NAME(S) AND ADDRESS(ES)
National Aeronautics and Space Administration
Washington, DC 20546-0001

10. SPONSORING/MONITOR'S ACRONYM(S)
NASA

11. SPONSORING/MONITORING REPORT NUMBER
NASA/TM–2005-213454

12. DISTRIBUTION/AVAILABILITY STATEMENT
Unclassified — Unlimited   Distribution: Nonstandard
Subject Category: 20, 34
Availability: NASA CASI (301) 621-0390

13. SUPPLEMENTARY NOTES
POC: Cetin C. Kiris, Ames Research Center, MS T27B-1, Moffett Field, CA 94035-1000
(650) 604-4485

14. ABSTRACT In phase II, additional inducer rotations are simulated in order to understand the root cause of the flowliner crack problem. CFD results confirmed that there is a strong unsteady interaction between the backflow regions caused by the LPFTP inducer and secondary flow regions in the bellows cavity through the flowliner slots. It is observed that the swirl on the duct side of the downstream flowliner is stronger than on the duct side of the upstream flowliner. Due to this swirl, there are more significant unsteady flow interactions through the downstream slots than those observed in the upstream slots. Averaged values of the local velocity at the slots were provided to the NESC-ITA flow physics acoustics team to guide them in designing the acoustics experiment. A parametric study was performed to compare the flow field in the flowliner area when one upstream slot and one corresponding downstream slot were enlarged. No significant differences were observed between the flow field obtained from the enlarged slot configuration when compared with the original configuration. More cases must be analyzed with various enlarged slot configurations to generalize this observation. The flow through the A1 test stand and the flow through the orbiter fuel feedline manifold were simulated without the LPFTP. It was observed that incoming flow to the flowliner and inducer was more uniform in the A1 test stand then in the orbiter manifold. Additionally, each engine LPFTP in the orbiter receives significantly different velocity distributions. Because of the differences observed in the computed results, it is not possible for the A1 test stand to represent the three different engine feedlines simultaneously.

15. SUBJECT TERMS
Low pressure fuel pumps, Incompressible flows, Computational fluid dynamics, Unsteady flows, Overset grid systems, Navier-Stokes equations, Time-accurate solutions

16. SECURITY CLASSIFICATION OF:			17. LIMITATION OF ABSTRACT	18. NUMBER OF PAGES	19a. NAME OF RESPONSIBLE PERSON
a. REPORT	b. ABSTRACT	c. THIS PAGE			Cetin C. Kiris
Unclassified	Unclassified	Unclassified	Unclassified	23	19b. TELEPHONE *(Include area code)* (650) 604-4485

Standard Form 298 (Rev. 8-98)
Prescribed by ANSI Std. Z39-18